GOETHE UNIVERSITÄT FRANKFURT AM MAIN

Master Thesis

Hybrid Static Potentials in SU(2) Yang-Mills Theory on the Lattice

Philipp Wolf

Institut für Theoretische Physik
Johann Wolfgang Geothe-Universität
Frankfurt am Main

March 2015

Supervisor: Prof. Marc Wagner
Second Supervisor: Prof. Owe Philipsen

Eigenständigkeitserklärung

Nach §30 (12) der Studienordnung der Goethe-Universität Frankfurt am Main für den Bachelor- und Masterstudiengang Physik vom 24.04.2013 versichere ich, dass diese Arbeit von mir selbstständig und ohne Benutzung anderer als der angegebenen Quellen und Hilfsmittel verfasst wurde. Ferner erkläre ich, dass diese Arbeit, auch nicht auszugsweise, für eine andere Prüfung oder Studienleistung verwendet worden ist.

Frankfurt am Main, den 31. März 2015

Philipp Wolf

Abstract. In this work static hybrid potentials are computed using SU(2) Yang-Mills theory on the lattice. The hybrid potentials are realized by local insertions of chromomagnetic or chromoelectric field operators in the midpoint of a quark antiquark pair. Two computations with different lattice spacings, $a \approx 0.073$ fm and $a \approx 0.038$ fm, have been performed yielding static hybrid potentials of the states Σ_g^+, Π_u, Σ_u^- and Σ_g^-.

Zusammenfassung. In dieser Arbeit werden statische Hybrid Potentiale mit der SU(2) Yang-Mills Theorie auf dem Gitter berechnet. Die Hybrid Potentiale werden mit Hilfe von lokalen Einfügungen chromomagnetischer und chromoelektrischer Feld-Operatoren zwischen dem Quark-Antiquark-Paar realisiert. Es wurden zwei Rechnungen mit unterschiedlichen Gitterabständen, $a \approx 0.073$ fm und $a \approx 0.038$ fm, für die statischen Hybrid Potentiale der Zustände Σ_g^+, Π_u, Σ_u^- und Σ_g^-, durchgeführt.

Contents

1 Introduction

In particle physics, hadrons are classified by the quark model, which also gives rise to their quantum numbers. A meson, for instance, can be identified with J^{PC}, where J, P and C denote the total angular momentum, parity and charge conjugation. Since, according to the quark model, the meson is a quark antiquark state, the quantum numbers are restricted to $P = (-1)^{L+1}$ and $C = (-1)^{L+S}$, with $S = 0, 1$ and $L = 0, 1, 2, \ldots$, which are denoting the spin and orbital angular momentum of the quark antiquark pair. A hybrid meson describes a state, which consists of a quark antiquark pair and some non-trivial excited gluon field, which contributes to the overall quantum numbers. Thus, a hybrid meson can carry quantum numbers beyond the ones dictated by the quark model. Such exotic states are for example, $J^{PC} = 0^{+-}, 0^{--}, 1^{-+}, \ldots$.

At present, exotic states are a hot topic in experimental particle physics. For instance the PANDA experiment at FAIR is aiming to search for gluonic excitations, e.g. glueballs and hybrid mesons. So far, the $J^{PC} = 1^{-+}$ states $\pi_1(1400)$ and $\pi_1(1600)$ are possible candidates for hybrid mesons or tetraquark states [1].

To shed some light into the physics of the hybrid mesons, an initial approach is the analysis of hybrid static potentials. Therefore, an infinitely heavy quark and antiquark, which are connected by an excited gluon field are considered. Similar to the computation of the static quark antiquark potential, the hybrid static potentials can be determined with Wilon loop-like observables using lattice QCD. This requires the introduction of additional gluonic operators, which take the quantum numbers of the excited gluon field into account. In this work chromomagnetic and chromoelectric field operators were inserted in the midpoint of the Wilson lines. Especially for hybrid mesons with heavy valence quarks, the static hybrid potentials can provide an estimate for their masses.

Based on earlier lattice studies, cf. [2, 3, 4, 5, 6, 8, 7, 9, 10, 11, 12, 13, 14, 15], hybrid static potentials will be computed in SU(2) Yang-Mills theory. Furthermore, in the context of effective field theories like pNRQCD there is particular interest in the

short distance behavior of hybrid static potentials, which is related to gluelump masses [15, 16]. For this purpose, two calculations with different lattice spacings, $a \approx 0.073$ fm and $a \approx 0.038$ fm, will be performed.

First of all, the theoretical aspects of this work are presented, which also include numerical issues and matters of implementation. Starting with a brief overview on spectroscopy in lattice QCD, the discussion will focus on the implementation of hybrid static potentials, which is based on the computation of Wilson loops. Afterwards, the results will be presented and discussed.

2 Theory

Quantum Chromodynamics (QCD) is a well-established theory describing the properties of the strong force, i.e. interactions between quarks and gluons, within the standard model of particle physics. The action of the theory is invariant under transformations of the non-abelian SU(3) gauge group. In consequence, gluons self interact with each other, and therefore particles exclusively made of gluons, like e.g. glueballs, are possible. Since for low energies the coupling constant of QCD is rather large than compared to QED, perturbative approaches will not work in this energy regime. Lattice gauge theory provides a non-perturbative way to perform QCD calculations. By discretizing space-time, path integrals of the continuum theory can be computed with Monte-Carlo methods.

The calculations in this work are performed in SU(2) Yang-Mills theory, which is a non-abelian gauge theory of the SU(2) group. Instead of postulating a local invariance of the Lagrangian under SU(3) transformations, like QCD does, one demands this invariance for the SU(2) group. Since this theory has similar properties as QCD, for instance confinement, and is much faster in lattice computations, SU(2) calculations are often the first step for lattice calculations. Afterwards, successful computations can be enhanced to full QCD with moderate effort.

It must be mentioned, that all equations in this work are in euclidian time, which is crucial for numerical calculation. Otherwise the integrands of the path integrals would be oscillating with a complex exponential function. The Wick rotation of the time to the complex axis: $t \to -i\tau$ leads to an exponential decay of the integrand, which allows a numerical treatment.

2.1 Spectroscopy on the lattice

To compute masses on the lattice one has to evaluate the correlation function $C(T)$ of a suitable operator, which can be calculated by solving a path integral on the lattice. The integration measure $\mathcal{D}[A_\mu, \psi, \bar{\psi}]$ implies an integration over all possible quark- and

gauge field configurations.

$$C(T) = \langle\Omega|\mathcal{O}^\dagger(T)\mathcal{O}(0)|\Omega\rangle = \frac{1}{Z}\int \mathcal{D}[A_\mu,\psi,\bar{\psi}]\mathcal{O}^\dagger(T)\mathcal{O}(0)e^{-S_{QCD}}[A_\mu,\psi,\bar{\psi}] \tag{2.1}$$

The operator $\mathcal{O}$, which is acting on the QCD vacuum state $|\Omega\rangle$, must be chosen in such way that it creates a state with the quantum numbers of the particle of interest. By using the euclidian time evaluation of the Operator $\mathcal{O}(T) = e^{\hat{H}T}\mathcal{O}(0)e^{-\hat{H}T}$ and inserting a set of energy eigenvalues one finds:

$$\begin{aligned}\langle\Omega|\mathcal{O}^\dagger(T)\mathcal{O}(0)|\Omega\rangle &= \sum_n \langle\Omega|e^{HT}\mathcal{O}^\dagger(0)e^{-HT}|n\rangle\langle n|\mathcal{O}(0)|\Omega\rangle \\ &= \sum_n |\langle n|\mathcal{O}(0)|\Omega\rangle|^2 e^{-(E_n-E_\Omega)T}\end{aligned} \tag{2.2}$$

Observing eq. (2.2) one notices that for large time separations T only the first term of the sum has a non-negligible contribution, because the energy differences increase by rising n. Identifying the energy difference between the first excited state and the QCD vacuum as the mass $m = E_0 - E_\Omega$ of the particle, one finds an exponential decay for the considered mass, cf. eq. (2.3).

$$C(T) = |\langle 0|\mathcal{O}(0)|\Omega\rangle|^2\ e^{-mT}, \quad \text{for large T} \tag{2.3}$$

Having a closer look at the expansion of the correlation function, eq. (2.2), it appears that not only large time separations are essential for suppressing the higher terms. Furthermore it is necessary that the overlap of the trial state $\mathcal{O}|\Omega\rangle$ and the ground state $\langle 0|$ is large compared to the higher overlaps. In general it is sufficient that the operator $\mathcal{O}$ satisfies certain symmetry properties which characterize the quantum numbers of the considered particle, as mentioned before. But for numerical computations a large overlap to the ground state can also be crucial to get a clear signal. Otherwise one would have to go to much higher time separations, which can cost a lot of computation time. As the choice of a suitable operator is arbitrary except for the symmetries and gauge invariance, it is a non-trivial task to find an operator, which leads to a reasonable amount of computation time.

If the correlation function has been computed successfully, the next step is to extract the mass. One possibility is to fit an exponential function to the correlation function,

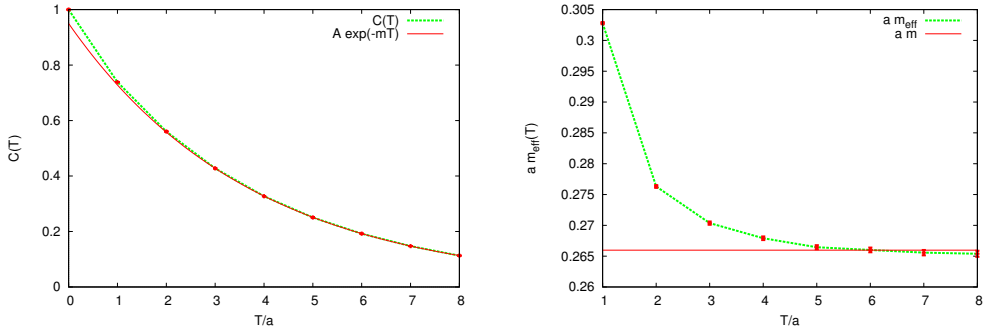

Figure 2.1: **(left)** Fitting an exponential function to the correlation function $C(T)$. **(right)** Fitting a constant to the effective mass for large time separations. (*The plots show the correlation function and effective mass of an ordinary Wilson loop with spatial extension* $R/a = 5$.)

which should match for large T, cf. figure 2.1 (left). But it is more common to analyze a quantity which is called effective mass.

$$m_{\text{eff}}(T) = \frac{1}{a} \ln \left(\frac{C(T)}{C(T+a)} \right) \tag{2.4}$$

Since the correlation function will follow an exponential decay for large T, the effective mass will become a constant at these time separations. This behavior can be observed in figure 2.1 (right).

$$m_{\text{eff}}(T) \;\rightarrow\; m, \quad \text{for large T} \tag{2.5}$$

2.2 The static quark antiquark potential

The static potential of a quark antiquark pair is a quite common and important observable in lattice QCD. It is defined as the energy between a static quark and antiquark as a function of the spatial separation R of the quarks. In this context static means that the quarks are located at a certain lattice site. This can be realized by considering the quarks in the limit of infinitely heavy masses. As a consequence of this the static quarks can be treated as spinless color sources.

The static potential is often computed to set the scale in lattice calculations. Since all lattice observables are dimensionless, a scale is needed to relate them to physical quantities. Since the potential becomes linear, $\backsim \sigma R$ for large R, the string tension σ can be compared to its physical value, which is typically about $\sigma \approx 5.5/\text{fm}^2 \ldots 7.5/\text{fm}^2$. In this way, the lattice spacing a can be determined for the given lattice calculation.

Another interesting feature of the static potential is, that it reveals the confining property of QCD. As mentioned before the potential has a linear slope for large R (cf. fig. 2.2 (right)), which means the energy rises by separating the quark antiquark pair. This behavior confirms the fact that quarks have never been observed separately. If also dynamical quarks would be taken into account the potential would show a saturation after the linear incline, which follows from a possible particle creation, if the energy of the separated quarks is high enough.

To compute the potential one usually uses the following creation operator,

$$\mathcal{O} = \bar{Q}(\mathbf{x})\mathcal{S}(\mathbf{x},\mathbf{y})Q(\mathbf{y}), \quad \text{with} \ \ |\mathbf{x}-\mathbf{y}| = R \tag{2.6}$$

where $\bar{Q}(\mathbf{x})$ and $Q(\mathbf{y})$ are creating a static antiquark and quark at the lattice sites $\mathbf{x}$ and $\mathbf{y}$. $\mathcal{S}(\mathbf{x},\mathbf{y})$ is a product of gauge links connecting the two quark fields in order to ensure gauge invariance of the operator.
In the limit of infinitely heavy quarks the integration over the quark fields in the integral (2.1) can be carried out analytically, cf. [17] for details. Finally the result is a path integral of the so-called Wilson loop $W(R,T)$, which is weighted by the gluonic Yang-Mills action S_G and integrated over all possible configurations of the gauge field A_μ.

$$C(T) \propto \langle W(R,T)\rangle \equiv \frac{1}{Z}\int \mathcal{D}[A_\mu]W(R,T)e^{-S_G[A_\mu]}, \quad S_G = \frac{1}{2}\mathrm{Tr}\int \mathrm{d}^4x F_{\mu\nu}F_{\mu\nu} \tag{2.7}$$

Another approach to this equation can be found in [18], where the inverse dirac propagator is expanded in a quantity, which is inverse proportional to the quark mass. In the end it turns out that for large masses the leading order of this expansion is just a simple Wilson line, which will be defined below. This procedure is known as the hopping expansion of the dirac propagator.

Definition of the Wilson loop

The Wilson loop is the trace of a product of gauge link variables, which are forming a rectangle with one axis in the time direction and one in spatial direction. One can structure it in four parts, two Wilson lines $\mathcal{S}(\mathbf{x},\mathbf{y};t)$, which are links in spatial directions and two temporal transporters $\mathcal{T}(\mathbf{x};t_1,t_2)$, which are connected in time direction, cf. fig. 2.2 (left).

$$\mathcal{S}(\mathbf{x},\mathbf{y};t) = \prod_{j=0}^{R/a-1} U_k(\mathbf{x}+ja\mathbf{e}_k,t), \quad \mathcal{T}(\mathbf{x};t_1,t_2) = \prod_{j=0}^{T/a-1} U_0(\mathbf{x},t_1+ja) \tag{2.8}$$

The Wilson loop can then be written as

$$W(R,T) = \mathrm{Tr}\left(\mathcal{S}(\mathbf{x},\mathbf{y};0)\mathcal{T}(\mathbf{y};0,t)(\mathcal{S}(\mathbf{x},\mathbf{y};t))^\dagger(\mathcal{T}(\mathbf{x};0,t))^\dagger\right) \tag{2.9}$$

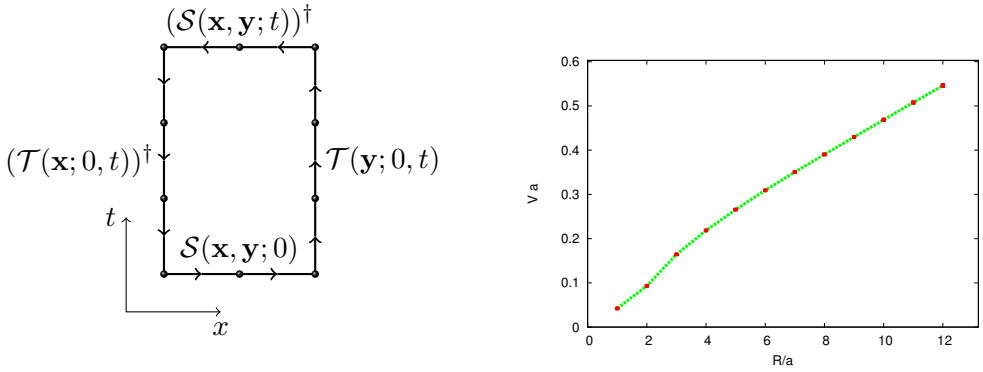

Figure 2.2: **(left)** Wilson loop $W(R,T)$ in the (x,t)-plane with $R = 2$ and $T = 3$. **(right)** Static quark antiquark potential, computed with Wilson loops.

As discussed in the previous section, the static potential can be determined by evaluating the effective mass or effective potential $V_{\mathrm{eff}}(R,T)$ for large time separations.

$$V_{\mathrm{eff}}(R,T) = \frac{1}{a}\ln\left(\frac{\langle W(R,T)\rangle}{\langle W(R,T+a)\rangle}\right) \tag{2.10}$$

2.3 Hybrid static potentials

Like the ordinary static potential the hybrid static potential is a construct of a static quark and antiquark, but furthermore the gluons can carry certain quantum numbers. The computation of the static potential was based on the evaluation of the Wilson loops. In case of a hybrid potential it is necessary to modify these Wilson loops in order to take the additional quantum numbers of the gluons into account.
One possible way is to insert a chromomagentic or chromoelectric field tensor $\mathbf{B},\mathbf{E}$ in the middle of the Wilson line, cf. fig. 2.3 a). This insertion can change the overall quantum number of the potential, which leads to a hybrid potential. Depending on the symmetry properties of this insertion, different hybrids can be created. This will be discussed more

precisely in the following.

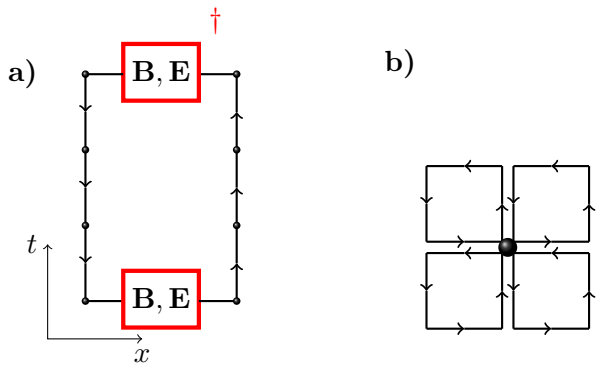

Figure 2.3: **a)** Generalized Wilson loop, which has $\mathbf{B}, \mathbf{E}$ field insertions in between the midpoint of the quark antiquark pair. **b)** clover plaquette: sum over four plaquettes with equal orientations, which are starting in the same point.

2.3.1 Gluonic operators on the lattice

The **B** and **E** field operators are defined analog to the definition known from electrodynamics.

$$B^l = -\frac{1}{2}\varepsilon^{lij}F^{ij}, \qquad E^i = F^{i0} \tag{2.11}$$

Therefore the insertions are proportional to the field strength tensor $F^{\mu\nu}$, which can be implemented with the so-called *clover plaquette* on the lattice, cf. fig. 2.3 b). To see this, one can perform a Taylor-expansion of the plaquette $U_{\mu\nu}$ for small lattice spacings a.

$$\begin{aligned} U_{\mu\nu}(n) &= e^{iga^2 F_{\mu\nu}(n)} = \mathbb{1} + iga^2 F_{\mu\nu} + \mathcal{O}(a^4) \\ U^\dagger_{\mu\nu}(n) &= e^{-iga^2 F_{\mu\nu}(n)} = \mathbb{1} - iga^2 F_{\mu\nu} + \mathcal{O}(a^4) \\ \longrightarrow \quad F_{\mu\nu}(n) &= \frac{1}{2iga^2}\left(U_{\mu\nu}(n) - U^\dagger_{\mu\nu}(n)\right) + \mathcal{O}(a^2) \end{aligned} \tag{2.12}$$

Since the computation of the mass depends only on the exponential decay rate, the prefactor $1/2iga^2$ does not matter and can be left out. Thus, the calculation of the field strength tensor simplifies to $U_{\mu\nu} - U^\dagger_{\mu\nu}$, for small lattice spacings.
A further improvement can be achieved by using the clover plaquette $Q_{\mu\nu}$ instead of the ordinary plaquette.

$$Q_{\mu\nu}(n) = \frac{1}{4}\left(U_{\mu\nu}(n) + U_{\nu-\mu}(n) + U_{-\mu-\nu}(n) + U_{-\nu\mu}(n)\right) \tag{2.13}$$

One benefit is that the clover plaquette enhances the statistics, as it averages over four ordinary plaquettes, another advantage will be seen when the lattice version of the derivative of the field strength tensor is discussed.

Derivative of the field strength tensor

The gluonic operators of the hybrid potentials can also contain derivatives of the field strength tensor. Using the discretized derivative on the lattice it follows with eq. (2.12)

$$\begin{aligned} C_{\mu\nu} \equiv D_\mu F_{\mu\nu}(n) &= -\frac{1}{a}\Big[F_{\mu\nu}(n - ae_\mu) - F_{\mu\nu}(n)\Big] + \mathcal{O}(a) \\ &= -\frac{1}{2iga^3}\Big[U_{\mu\nu}(n - ae_\mu) + U^\dagger_{\mu\nu}(n) \\ &\quad - \Big(U_{\mu\nu}(n - ae_\mu) + U^\dagger_{\mu\nu}(n)\Big)^\dagger\Big] + \mathcal{O}(a) \end{aligned} \tag{2.14}$$

Again the prefactor $-1/2iga^3$ has no effect on the computation of the hybrid potential and can be neglected. The derivative $C_{\mu\nu}$ is not constructed *gauge invariant* yet. Under a gauge transformation g, the following behavior is required:

$$D_\mu F_{\mu\nu}(n) \xrightarrow{\quad g \quad} g(n)\; D_\mu F_{\mu\nu}(n)\; g^\dagger(n)$$

For each of the plaquettes $U_{\mu\nu}$ in eq. (2.14) this transformation law is separately fulfilled, but as they are situated at different lattice sites the sum of them cannot be gauge invariant. By multiplying two link variables from the left and right to the first plaquette, the requested transformation property can be achieved. Respectively, $\widetilde{C}_{\mu\nu}$ represents a possible implementation of the covariant derivative of $F_{\mu\nu}$ on the lattice.

$$\begin{aligned} \widetilde{C}_{\mu\nu} =& \Big(U^\dagger_\mu(n - ae_\mu)\; U_{\mu\nu}(n - ae_\mu)\; U_\mu(n - ae_\mu) + U^\dagger_{\mu\nu}(n)\Big) \\ &- \Big(U^\dagger_\mu(n - ae_\mu)\; U_{\mu\nu}(n - ae_\mu)\; U_\mu(n - ae_\mu) + U^\dagger_{\mu\nu}(n)\Big)^\dagger \end{aligned} \tag{2.15}$$

Fig. 2.4 shows the visualization of the first line of eq. (2.15). Since the red link and the first link of the black plaquette cancel each other, the plaquette starts now in n, proceeding counter-clockwise until it is closed with the blue link. The second term in the sum is the green daggered plaquette, which is an ordinary plaquette with clockwise

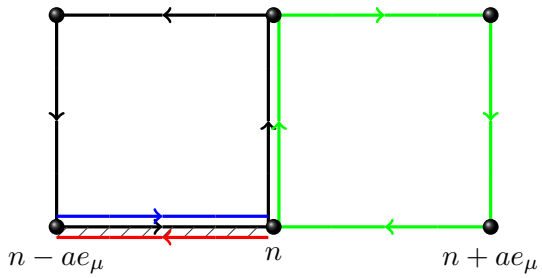

Figure 2.4: Corresponds to the first line of eq. (2.15). The result is a sum of two plaquettes starting in the same point, but with different orientations.

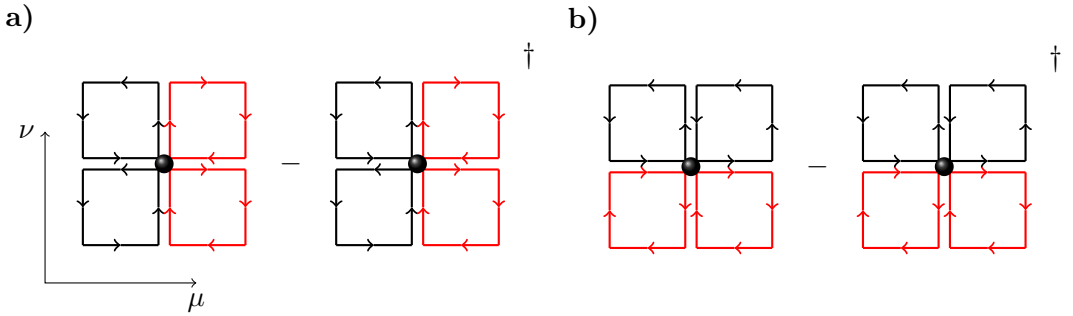

Figure 2.5: **a)** Derivative of $F_{\mu\nu}$ with respect to the μ-direction. **b)** Derivative of $F_{\mu\nu}$ with respect to the ν-direction. *Note that all clover plaquettes are situated at the same lattice site. The red colored plaquettes indicate a clockwise orientation.*

orientation. Altogether one has to sum up two plaquettes, which are starting in n and having different orientations. For $\widetilde{C}_{\mu\nu}$ the daggered of this object has to be subtracted in the end, like eq. (2.15) demands.
This operator can also be improved to a kind of clover leaf structured object. For this purpose, two additional plaquettes with starting points in n are added. It is important that the orientations of the plaquettes differ along the direction of the derivative, cf. fig. 2.5. The advantage is again the higher statistics, but now another benefit can be seen. If only one plaquette would be used to implement $F_{\mu\nu}$, this operator might have an overlap to the derivative of $F_{\mu\nu}$, as the operator of the derivative consists of the same plaquette. By adding the additional plaquettes the two operators get more distinguishable, hence they should create states with less contributions from other sectors.

So far the discussion was limited to the case that the directional derivative lies in the plane of the field strength tensor. Since the procedure in the other case is analog

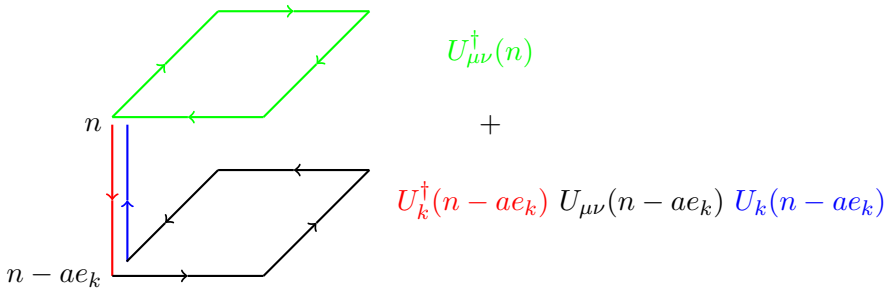

Figure 2.6: Corresponds to the first line of eq. (2.15), for the case that the derivative direction is perpendicular to $F_{\mu\nu}$.

to the one discussed above, it will not be explained in detail. Basically, the difference is that the plaquettes, which are summed up, are no longer situated side by side, as seen in fig. 2.4. Now they are positioned adverse to each other. Fig. 2.6 shows the corresponding illustration for the first line of eq. (2.15), in case that the derivation direction is perpendicular to the plane of $F_{\mu\nu}$. Again, this operator can be extended to a clover like operator, as done before.

2.3.2 Modified Wilson loops with even spatial extension

If a Wilson loop has an even spatial separation, it is not possible to insert a gluonic operator directly in the midpoint, as it was shown in fig. 2.3 (left). Since there is no lattice site in the middle, the insertion $\mathcal{I}$ could be placed half a lattice spacing to the right (operator $\mathcal{O}_R$), or left (operator $\mathcal{O}_L$) from the midpoint.

$$\mathcal{O}_L(t) \equiv \prod_{j=0}^{\lfloor R/2a \rfloor - 1} U_k(\mathbf{x} + aj\mathbf{e}_k, t)\ \mathcal{I}(\mathbf{x} + \lfloor R/2 \rfloor\ \mathbf{e}_k, t) \prod_{\lfloor R/2a \rfloor}^{R/a-1} U_k(\mathbf{x} + aj\mathbf{e}_k, t) \tag{2.16}$$

$$\mathcal{O}_R(t) \equiv \prod_{j=0}^{\lfloor R/2a \rfloor} U_k(\mathbf{x} + aj\mathbf{e}_k, t)\ \mathcal{I}(\mathbf{x} + (\lfloor R/2 \rfloor + a)\mathbf{e}_k, t) \prod_{\lfloor R/2a \rfloor + 1}^{R/a-1} U_k(\mathbf{x} + aj\mathbf{e}_k, t) \tag{2.17}$$

But this would change the symmetry properties of the operator, and thus, the operator could create states that have contributions from other sectors. To avoid this, it is possible to average over both operators. The new operator $\mathcal{O}_{LR}(t) = 1/2(\mathcal{O}_L(t) + \mathcal{O}_R(t))$ keeps the symmetries, but in return, four different Wilson loops have to be calculated.

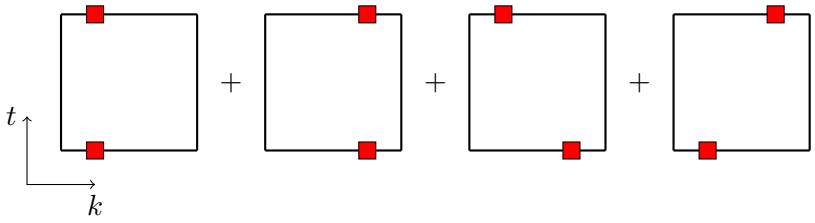

Figure 2.7: Sum of four modified Wilson loops, corresponding to eq. (2.18). The red rectangles denote the position of the gluonic insertions.

$$\begin{aligned}\langle\Omega|\left(\mathcal{O}_L(t)+\mathcal{O}_R(t)\right)^\dagger\left(\mathcal{O}_L(0)+\mathcal{O}_R(0)\right)|\Omega\rangle& \\ = \langle\Omega|\mathcal{O}_L^\dagger(t)\mathcal{O}_L(0)|\Omega\rangle + \langle\Omega|\mathcal{O}_R^\dagger(t)\mathcal{O}_R(0)|\Omega\rangle& \\ + \langle\Omega|\mathcal{O}_L^\dagger(t)\mathcal{O}_R(0)|\Omega\rangle + \langle\Omega|\mathcal{O}_R^\dagger(t)\mathcal{O}_L(0)|\Omega\rangle& \end{aligned} \tag{2.18}$$

An illustration of eq. (2.18) can be seen in fig. 2.7.

2.4 Quantum numbers of hybrid potentials

In the previous section the lattice implementation of **B** and **E** field operators and their derivatives have been discussed. Inserting these operators into the Wilson loops, as suggested before, will dictate the quantum numbers of the potential. Depending on the symmetry properties of the insertion itself and their orientation with respect to the separation axis of the quark antiquark pair, different quantum numbers can be obtained. The static hybrid potentials are classified by three different quantum numbers [11].

- The angular momentum with respect to the separation axis **R**. This corresponds to a rotation around the separation axis. Potentials with $J_R = 0, 1, 2, ...$ are labeled with $\Sigma, \Pi, \Delta, ...$
- The combination of parity P and charge conjugation C. States with $P \circ C = +(-)$ are labeled with $g(u)$ in subscript.
- The rotational invariant Σ states have an additional quantum number $\mathcal{P}_x = +(-)$, which depends on spatial reflections along an axis, which is perpendicular to the

separation axis.

quantum numbers $J^{P_x}_{P\circ C}$	operator insertions
Σ_g^+	$1 \quad , \quad \mathbf{R}\cdot\mathbf{E} \quad , \quad \mathbf{R}\cdot(\mathbf{D}\times\mathbf{B})$
Π_g	$\mathbf{R}\times\mathbf{E} \quad , \quad \mathbf{R}\times(\mathbf{D}\times\mathbf{B})$
Σ_u^-	$\mathbf{R}\cdot\mathbf{B} \quad , \quad \mathbf{R}\cdot(\mathbf{D}\times\mathbf{E})$
Π_u	$\mathbf{R}\times\mathbf{B} \quad , \quad \mathbf{R}\times(\mathbf{D}\times\mathbf{E})$
Σ_g^-	$(\mathbf{R}\cdot\mathbf{D})(\mathbf{R}\cdot\mathbf{B})$

Table 2.1: Quantum numbers of static hybrid potentials [11].

Tab. 2.1 shows different gluonic creation operators and the corresponding quantum numbers. The **B** and **E** fields can be combined with the unit vector **R** of the separation axis and the covariant derivative **D**.
To understand the general procedure, how these quantum numbers are realized by the operators of tab. 2.1, the operators $\mathbf{R}\cdot\mathbf{E}$ and $\mathbf{R}\cdot\mathbf{B}$ are discussed.

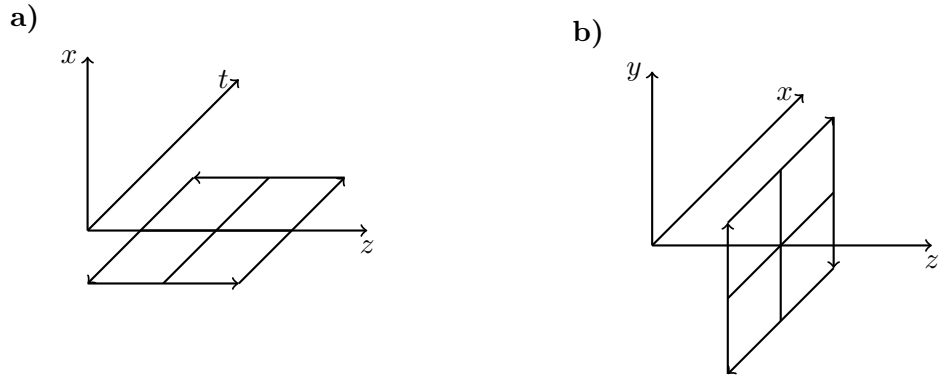

Figure 2.8: **a)** $\mathbf{R}\cdot\mathbf{E}$, with $\mathbf{R} = (0,0,1)^T$; the clover plaquette lies in the (z,t)-plane.
b) $\mathbf{R}\cdot\mathbf{B}$ with $\mathbf{R} = (0,0,1)^T$; the clover plaquette lies in the (x,y)-plane.

Angular momentum

In the case of $\mathbf{R}\cdot\mathbf{E}$ and $\mathbf{R}\cdot\mathbf{B}$ the angular momentum is zero $J_R = 0$, as the operators are rotational invariant around the separation axis, c.f. fig. 2.8.

In addition the angular momentum of $\mathbf{R}\times\mathbf{B}$ is discussed. Let z be the separation axis, thus $\mathbf{R}\times\mathbf{B} = (-B_y, B_x, 0)^T$. It will be shown that an insertion of B_y or B_x creates

a hybrid potential with angular momentum $J_z = 1$. For this purpose, we will first look at the combination $B_x \pm iB_y$ and show that this quantity has $J_z = \pm 1$.
Since B_x corresponds to a clover plaquette in the (z, y)-plane, it can be characterized by its normal vector $(1, 0, 0)^T$. Equivalently, one can identify B_y with $(0, 1, 0)^T$. Performing an infinitesimal rotation around the z-axis $\mathcal{D}_z(\alpha)$ of the operators leads to:

$$\mathcal{D}_z(\alpha) \cdot B_x = \begin{pmatrix} 1 & -\alpha & 0 \\ \alpha & 1 & 0 \\ 0 & 0 & 1 \end{pmatrix} \begin{pmatrix} 1 \\ 0 \\ 0 \end{pmatrix} = \begin{pmatrix} 1 \\ 0 \\ 0 \end{pmatrix} + \alpha \begin{pmatrix} 0 \\ 1 \\ 0 \end{pmatrix} = B_x + \alpha B_y$$

$$\mathcal{D}_z(\alpha) \cdot B_y = \begin{pmatrix} 1 & -\alpha & 0 \\ \alpha & 1 & 0 \\ 0 & 0 & 1 \end{pmatrix} \begin{pmatrix} 0 \\ 1 \\ 0 \end{pmatrix} = \begin{pmatrix} 0 \\ 1 \\ 0 \end{pmatrix} - \alpha \begin{pmatrix} 1 \\ 0 \\ 0 \end{pmatrix} = B_y - \alpha B_x$$

Now it is possible to investigate the behavior of $B_x \pm iB_y$ under the transformation $\mathcal{D}_z(\alpha)$.

$$B_x \pm iB_y \xrightarrow{\mathcal{D}_z(\alpha)} (B_x + \alpha B_y) \pm i(B_y - \alpha B_x) = (1 \mp i\alpha)(B_x \pm iB_y) \tag{2.19}$$

Considering $\mathcal{D}_z(\alpha)$ as a Lie-algebra, with L_z denoting the z component of the angular momentum operator, one finds:

$$\mathcal{D}_z(\alpha) \cdot (B_x \pm iB_y) = \exp(-i\alpha L_z)(B_x \pm iB_y) = (1 - i\alpha L_z + \mathcal{O}(\alpha^2))(B_x \pm iB_y) \tag{2.20}$$

Comparing eq. (2.19) with eq. (2.20), the eigenvalue of L_z can be identified.

$$(1 - i\alpha L_z)(B_x \pm iB_y) = (1 - i\alpha(\pm 1))(B_x \pm iB_y) \tag{2.21}$$

Therefore, the combinations $(B_x \pm iB_y)$ create gluonic excitations with $l_z = \pm 1$. Since both states have the same mass, also a superposition of them can be used to analyze a hybrid potential with $l_z = 1$. Two simple superpositions lead to the operators B_x and B_y, which do not have $l_z = 1$ any more, but still are exciting a sector, which corresponds to a hybrid potential with $l_z = 1$.

Parity and charge conjugation

To perform the parity transformation, the operator has to be reflected on all spatial axes with respect to the midpoint. Since the **E** field has one temporal and one spatial

extension (fig. 2.8 a)), the operator is only reflected at one single plane, which changes the orientation of the plaquettes, which again results in a change of sign. The **B** field has two spatial extensions, therefore it has to be reflected at two planes, which recovers the counter-clockwise orientation of the plaquettes.

$$\mathbf{E} \xrightarrow{\mathcal{P}} -\mathbf{E}, \qquad \mathbf{B} \xrightarrow{\mathcal{P}} \mathbf{B} \tag{2.22}$$

Since the gauge field transforms like $A_\mu \to -A_\mu^T$ under a charge conjugation, the links act like $U(x,y) \to U^T(y,x)$. Hence, the charge conjugation basically reverses all link variables, which causes again a change of sign.

$$\mathbf{E} \xrightarrow{\mathcal{P}\circ\mathcal{C}} \mathbf{E}, \qquad \mathbf{B} \xrightarrow{\mathcal{P}\circ\mathcal{C}} -\mathbf{B} \tag{2.23}$$

Additional quantum number $\mathcal{P}_x$

For the $\mathbf{R}\cdot\mathbf{E}$ operator the axis perpendicular to the separation axis corresponds to the x-axis in fig. 2.8 a). Thus, the reflection has no impact on the orientation of the plaquettes. In contrast, the $\mathbf{R}\cdot\mathbf{B}$ operator has to be reflected at the y- or x-axis, in the case of fig. 2.8 b), which causes a change of sign.

With similar considerations one can obtain the quantum numbers of the remaining operators in tab. 2.1.

2.4.1 Symmetry averaging and symmetry cross-checks

The symmetry properties of the operators can on the one hand be used to cross-check the results, and on the other, they can increase the statistics by averaging over correlation functions with the same quantum numbers.

Symmetry averaging

The notation of the gluonic operators shown in tab. 2.1 already suggests to average over different separation axes, as no axis is distinguished. Averaging in this context means computing the average of correlation functions with the same quantum numbers on each configuration. In the end, the average over the configurations is calculated as usual.

Tab. 2.2 shows that the Σ_u^- state can be improved by averaging over the correlation functions of B_z, B_y and B_x with respect to the certain separation axis. For the Π_u even six operators can be summed up.

separation axis	Σ_u^-	Π_u
z	B_z	B_x, B_y
y	B_y	B_x, B_z
x	B_x	B_y, B_z

Table 2.2: Gluonic **B** field creation operators with respect to the separation axis.

Fig. 2.9 shows two examples for this procedure. The plot on the left illustrates the effective potential of the operator B_x (blue curve), for the separation axis in x direction, and the effective potential of the average over all three operators with respect to their separation axis (green curve). The errors are expected to decrease by a factor of $\sqrt{3}$, which is almost fulfilled.
In the case of the Π_u state, two different operators can be averaged for each possible separation axis. Again, the green curve in the right plot shows the average of all six operators, while the blue one denotes just B_x, which was computed for a separation axis in z direction. This time, the errors should decrease by a factor of $\sqrt{6}$.

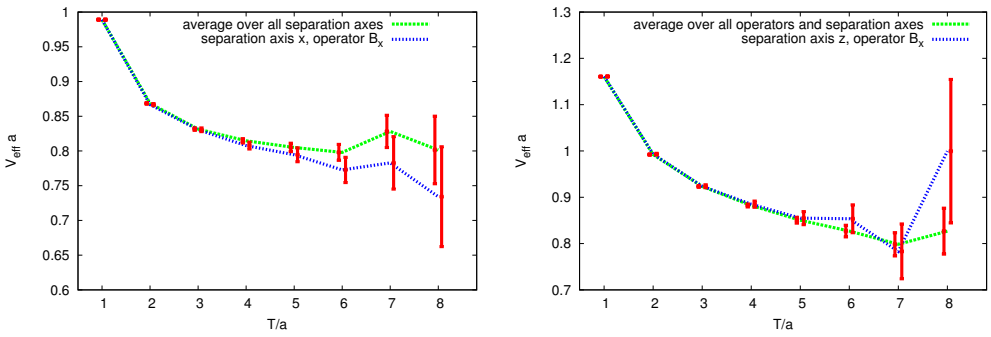

Figure 2.9: **(left)** $V_{\text{eff}}(R/a = 5, T)$ of $\mathbf{R} \cdot \mathbf{B}$ and **(right)** $V_{\text{eff}}(R/a = 12, T)$ of $\mathbf{R} \times \mathbf{B}$ for different correlation function averages. *To be able to distinguish between the different curves, the errorbars have slightly been shifted horizontally.*

Symmetry cross-checks

Before averaging over correlation functions, as done in the above example, it should be checked if the correlation functions are equal within statistical errors. Otherwise this could be an indication for a possible mistake in the program code or even a conceptual issue. Therefore, symmetry cross-checks are a powerful tool to proof the correctness of the calculations.

Beside investigating different separation axes, there are other symmetries, e.g. parity or time reversal, which can be cross-checked. For this purpose, the correlation functions of all operators $\langle\Omega|\mathcal{O}_i^\dagger(t)\mathcal{O}_j(0)|\Omega\rangle$ have to be computed, which of course include correlation functions containing two different operators. These are necessary to check parity and time reversal properties.
Since correlation functions of operators with different parity are zero, this property can be used to cross-check the computation. Fig. 2.10 (left) exemplifies one possible operator combination. For this plot, modified Wilson loops with the B_x operator as upper insertion and the identity as lower insertion, have been calculated. As B_x and 1 behave differently under parity transformation, the Wilson loop configuration average should be zero within errors, which can be observed.

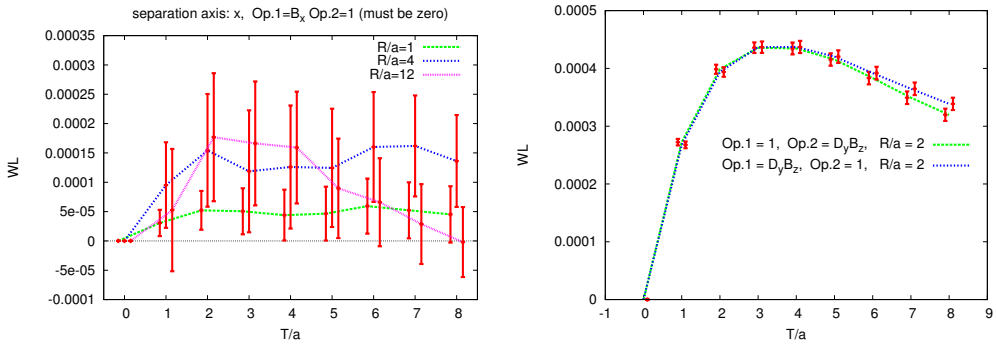

Figure 2.10: **(left)** Configuration average of a modified Wilson loop with upper insertion B_x and 1 as lower insertion. **(right)** Configuration average of a modified Wilson loop with upper insertion 1 and iD_yB_z as lower insertion, compared to the time reversed case. *To be able to distinguish between the different curves, the errorbars have slightly been shifted horizontally.*

Performing a time reversal $t \longmapsto -t$, the insertions in a modified Wilson loop swap with each other. Since two different operators are considered, and the upper insertion is daggered, the prefactors of the **B** and **E** field operators as discussed in eq. (2.12), cannot be neglected any more. It has to be taken into account that the insertions are proportional to $\backsim iF_{\mu\nu}$, as this influences the change of sign, by daggering.
Fig. 2.10 (right) illustrates such a time reversal cross-check. The green curve shows the configuration average of a Wilson loop with the identity as upper operator and an insertion of (iD_yB_z) at the bottom. This can be compared with the time reversed case (blue curve), which is now a Wilson loop with $(iD_yB_z)^\dagger$ inserted at the top and the identity as lower operator. Since $iD_yB_z \backsim iF_{xy}$ and $F_{xy}^\dagger = -F_{xy}$, we have $iD_yB_z = (iD_yB_z)^\dagger$.

Therefore both correlation functions should be equal within errors, which can clearly be seen.

The above mentioned reveals that it is reasonable to compute all correlation functions $\langle\Omega|\mathcal{O}_i^\dagger(t)\mathcal{O}_j(0)|\Omega\rangle$ of the possible operators,

$$\begin{aligned}\mathcal{O}_i^B &\in \{1, B_x, B_y, B_z, D_xB_x, D_xB_y, D_xB_z, D_yB_x, D_yB_y, D_yB_z, D_zB_x, D_zB_y, D_zB_z\}\\ \mathcal{O}_i^E &\in \{1, E_x, E_y, E_z, D_xE_x, D_xE_y, D_xE_z, D_yE_x, D_yE_y, D_yE_z, D_zE_x, D_zE_y, D_zE_z\}\end{aligned} \tag{2.24}$$

with respect to the separation axis. Afterwards several symmetry checks can be performed, and in the end the operators from tab. 2.1 can be built up from the single components from eq. (2.24).
For the **B** operators 13^2 correlation function combinations with 3 different separation axes can be computed on each configuration. Together with the **E** operators, more than thousand correlation functions will be calculated on a single configuration.

Remark about E field operators

It should be mentioned that the correlation functions of operators which contain **E** fields are negative, i.e. $C(T) \backsim -\exp^{-V(R)T}$. Since the chromoelectric field is the time derivative of the vector potential (in temporal gauge $A_0 = 0$), it can be shown[1] that our assumed **E** field operators have an additionally factor of $-i$, i.e. $U_{j0} - U_{j0}^\dagger = -i\hat{E}_j$.

[1] Similarly it can be shown that in QM $\frac{(\hat{x}(\varepsilon)-\hat{x}(0))}{\varepsilon} = -i\frac{\hat{p}}{m}$ holds.

3 Results

Two major calculations were realized to analyze the static hybrid potentials. The first one includes a computation of the modified Wilson loops with the gluonic operators from tab. 2.1, for a lattice spacing $a \approx 0.073$ fm. In a second computation of the static hybrid potentials the lattice spacing is halved, in order to analyze discretization effects by comparing both results.
In the following the two calculations are presented and discussed separately. Finally a comparison of both results is carried out.

3.1 Static hybrid potentials for $\beta = 2.5$

3.1.1 Lattice setup

Over 700 essentially independent gauge configurations with 24^4 lattice sites have been generated by using a heatbath algorithm. The configurations have been weighted with the SU(2) standard Wilson plaquette action. $\beta = 2.5$ corresponds to a lattice spacing of $a \approx 0.073$ fm, if the Sommer parameter r_0 is identified with 0.46 fm [19].

3.1.2 Effective potentials

Wilson loops and modified Wilson loops with spatial separations $R/a = 0, 1, 2, \ldots, 12$ and temporal separations $T/a = 0, 1, 2, \ldots, 8$ have been calculated on the generated gauge configurations. Over 1000 correlation functions, containing different gluonic operator combinations, were computed on each configuration, cf. (2.24). In the following, some representative examples of effective potentials are discussed to illustrate the main procedure of obtaining the potential from the computed correlation functions.

Ordinary static potential

Fig. 3.1 shows the effective potential and corresponding potential of the ordinary quark antiquark state without any gluonic excitation. In the region $T/a = 6 \ldots 8$ a constant is fitted to $V_{\text{eff}}(R, T)$, which is justified since the curves of $V_{\text{eff}}(R, T)$ seem to have reached

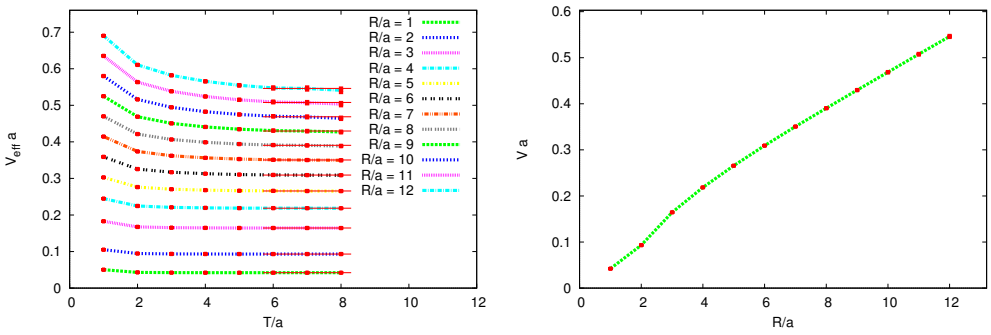

Figure 3.1: **(left)** Effective potential $V_{\text{eff}}(R,T)$ as a function of T for different quark antiquark separations R in units of the lattice spacing $a \approx 0.073\,\text{fm}$. **(right)** Static potential $V(R)$ in units of the lattice spacing.

the plateau for $T/a > 5$ or even smaller temporal separations.

Analyzing the effective potentials of the Wilson loops with gluonic insertions will be more challenging. Because of the additional insertions more link variables contribute and thus the errors increase. Another issue is the overlap with the ground state.

The static hybrid potentials $\mathbf{R} \times \mathbf{B}$, $(\mathbf{R}\cdot\mathbf{D})(\mathbf{R}\cdot\mathbf{B})$ and $\mathbf{R}\cdot\mathbf{E}$

Fig. 3.2, 3.3 and 3.4 show the effective potentials of the hybrids $\mathbf{R}\times\mathbf{B}$, $(\mathbf{R}\cdot\mathbf{D})(\mathbf{R}\cdot\mathbf{B})$ and $\mathbf{R}\cdot\mathbf{E}$. For clarity reasons, only even spatial separations are shown and the curves are separated into two plots. Compared to the ordinary potential, one notices significantly larger errorbars for higher temporal separations, which make it more complicated to fit the plateau. Furthermore, the effective potentials for smaller R/a decay faster to its plateau than the ones with larger separations. Especially fig. 3.2 shows quite well the mentioned behavior. The right plot shows $V_{\text{eff}}(R,T)$ for large separations, where the curves are still decaying, while the curves of the left plot are already in the plateau-like region. This might be a first hint, that the chosen operators of local $\mathbf{B}$ and $\mathbf{E}$ field insertions describe the hybrid potentials better for short ranged spatial separations, where the quark and antiquark pair is situated close to each other. But by increasing the distance, some operators appear to have a rather poor ground state overlap, and therefore, the effective masses have not reached the plateau for the considered temporal separation. Except for the $(\mathbf{R}\cdot\mathbf{D})(\mathbf{R}\cdot\mathbf{B})$ potential, all effective masses are fitted in the region $R/a = 6\ldots8$. Although the curves of the larger spatial separations slightly decrease by going to higher T/a, it is still reasonable to fit a constant to $V_{\text{eff}}(R,T)$ in the region

$T/a = 6 \ldots 8$, keeping in mind that the resulting potential $V(R)$ could be slightly too high for large R.

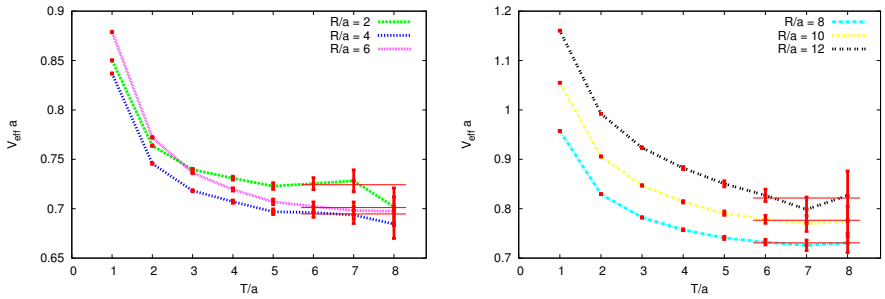

Figure 3.2: $V_{\text{eff}}(R, T)$ of the static hybrid potential $\mathbf{R} \times \mathbf{B}$

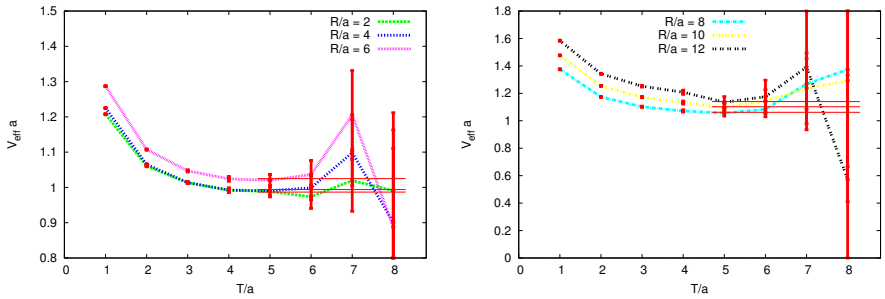

Figure 3.3: $V_{\text{eff}}(R, T)$ of the static hybrid potential $(\mathbf{R} \cdot \mathbf{D})(\mathbf{R} \cdot \mathbf{B})$.

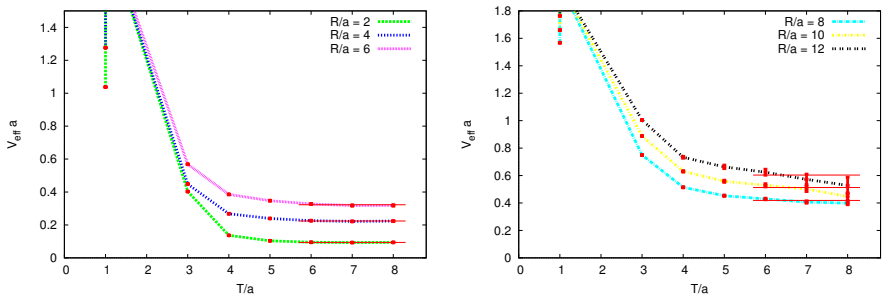

Figure 3.4: $V_{\text{eff}}(R, T)$ of the static hybrid potential $\mathbf{R} \cdot \mathbf{E}$. Has to be considered for $T/a > 2$.

The $(\mathbf{R}\cdot\mathbf{D})(\mathbf{R}\cdot\mathbf{B})$ operator seems to describe the ground state quite well, as $V_{\text{eff}}(R,T)$ reaches the plateau-like region for $T/a > 4$. Therefore the fit region can be shifted to $R/a = 5\ldots8$, which will improve the result for the potential.
Having a look at fig. 3.4 one notices an uncommon behavior of the effective mass for $T/a < 3$. This happens because the $\mathbf{E}$ field operator has a temporal extension. If the temporal extension of the modified Wilson loop is smaller than three, the $\mathbf{E}$ field insertions will overlap with each other creating some unphysical operator.

The static hybrid potential $\mathbf{R}\cdot(\mathbf{D}\times\mathbf{E})$

In fig. 3.5 the effective hybrid potential $\mathbf{R}\cdot(\mathbf{D}\times\mathbf{E})$ can be seen. Compared to the effective potentials before, it suffers from even higher statistical errors, and moreover it can not be clearly said if the plateau is already reached, or if higher temporal separations are needed. Since no data for larger temporal separations could be computed in a reasonable amount of time, $V_{\text{eff}}(R,T)$ is fitted from $R/a = 6\ldots8$. But in the analysis these results have to be treated with caution. Fortunately, the Σ_u^- state which is computed with the $\mathbf{R}\cdot(\mathbf{D}\times\mathbf{E})$ can also be obtained with the $\mathbf{R}\cdot\mathbf{B}$ operator, which has much smaller errors. Even though, the $\mathbf{R}\cdot(\mathbf{D}\times\mathbf{E})$ operator is not suited for a high precision calculation, it can serve as a cross-check.

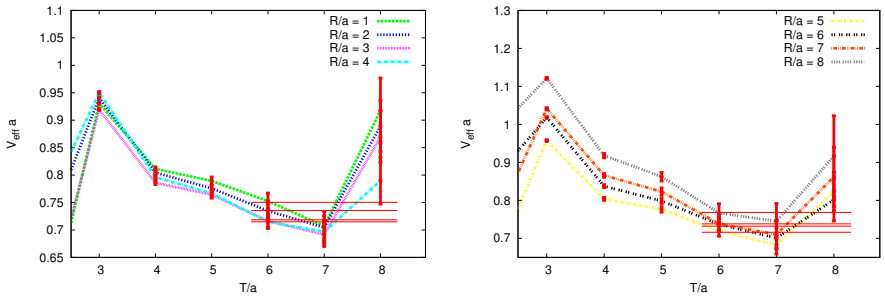

Figure 3.5: $V_{\text{eff}}(R,T)$ of the static hybrid potential $\mathbf{R}\cdot(\mathbf{D}\times\mathbf{E})$.

Like the $\mathbf{R}\cdot(\mathbf{D}\times\mathbf{E})$, some other gluonic operators, e.g. $\mathbf{R}\times(\mathbf{D}\times\mathbf{E})$ show a similar behavior, but there are also operators where no analysis was possible. For example the $\mathbf{R}\times\mathbf{E}$, which could not be evaluated, as the errorbars were much too large.

3.1.3 Potentials

Four different states have been computed, cf. fig. 3.6. For the states Σ_g^+, Π_u and Σ_u^- two gluonic creation operators have been evaluated, which lead to the same hybrid potential

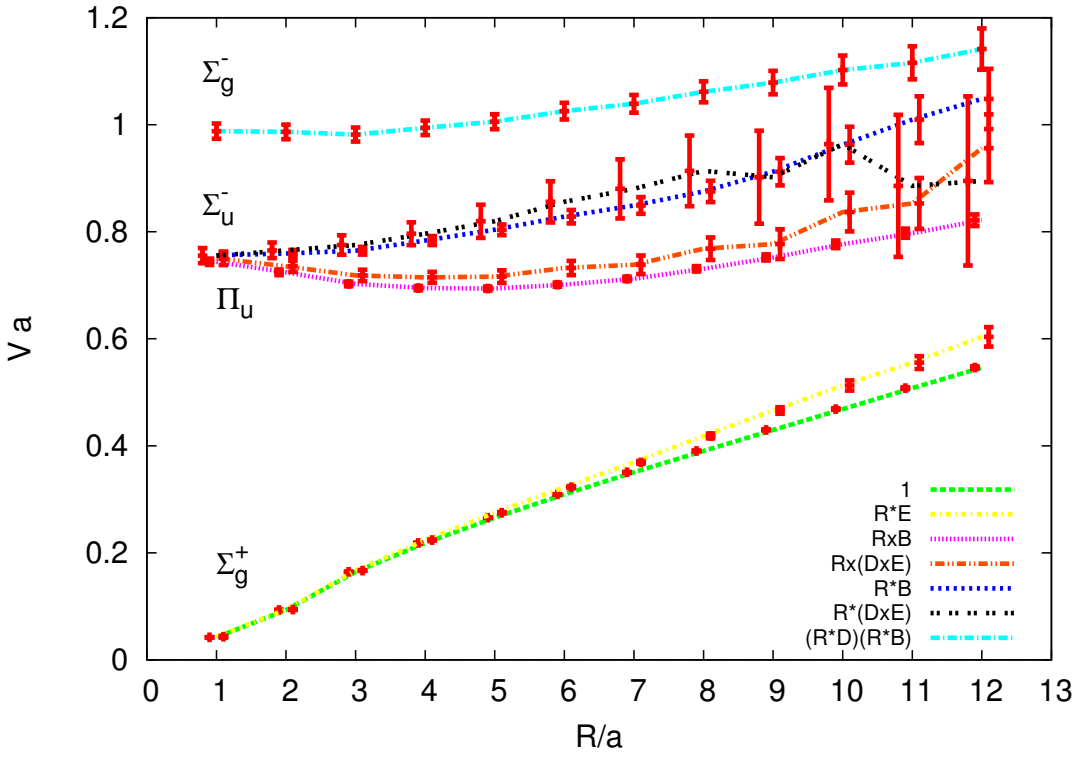

Figure 3.6: Hybrid static potentials in SU(2) Yang-Mills theory in units of the lattice spacing ($a \approx 0.073$ fm). *To be able to distinguish between the different curves, the errorbars have slightly been shifted horizontally.*

within statistical errors. For example the Σ_g^+ state has the same quantum numbers as the ordinary static quark antiquark potential (green curve), therefore the $\mathbf{R} \cdot \mathbf{E}$ potential (yellow curve) should match with the green curve. In the same way the magenta and the red curve are describing Π_u, while Σ_u^- is realized by the blue and black curve.
It appears that some operators are more suitable to describe a certain state than others, since the statistical errors are smaller, e.g. for the determination of the Σ_g^+, it is better to use the ordinary Wilons loops than the ones with $\mathbf{R} \cdot \mathbf{E}$ insertions. Equivalently, the $\mathbf{R} \times \mathbf{B}$ is more suitable than $\mathbf{R} \times (\mathbf{D} \times \mathbf{E})$ operator and the $\mathbf{R} \cdot \mathbf{B}$ superior to the $\mathbf{R} \cdot (\mathbf{D} \times \mathbf{E})$.

Comparing these results to earlier studies, e.g. [11], one notices that their errors are much smaller than the errors in this computation. One possible explanation for this might be the special choice of the creation operators, which is in our case a local insertion of $\mathbf{B}$ and $\mathbf{E}$ fields. Perhaps non-local operators which are extended over the whole Wilson

loop, as proposed in [6, 8], would have a higher ground state overlap than our current operators and therefore the effective potentials would reach the plateau-like region for smaller temporal separation.

3.2 Static hybrid potentials for $\beta = 2.7$

3.2.1 Lattice setup

Compared to section 3.1.1 the lattice setup is unchanged except for the lattice spacing. For $\beta = 2.7$ the lattice spacing corresponds to $a \approx 0.038$ [19], which is almost half the lattice spacing of the previous calculations.

3.2.2 Effective potentials

Again, ordinary and modified Wilson loops with spatial extensions $R/a = 0, 1, 2, \ldots, 12$ and temporal extensions $T/a = 0, 1, 2, \ldots, 8$ have been computed. This implies, that the physical length of both extensions is now halved. For this reason, some operators, especially for large R/a, are still dominated by excited states, since the temporal extension is not large enough. Fig. 3.7 exemplifies this issue quite well. For short separation distances the plateau seems to be reached, while for large separations this cannot be observed.

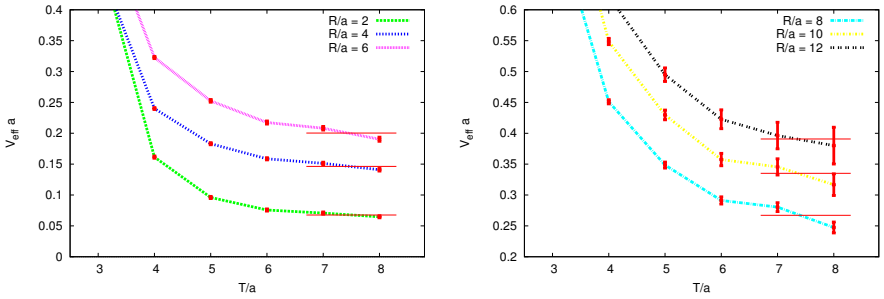

Figure 3.7: $V_{\text{eff}}(R, T)$ of the static hybrid potential $\mathbf{R} \cdot \mathbf{E}$ for $\beta = 2.7$.

By analyzing the different effective potentials, it can be observed that this effect is more distinctive for the operators containing $\mathbf{E}$ fields. The effective potentials of these operators reach the plateau-like region only for $T/a > 7$. Hence, the hybrid potentials from operators with $\mathbf{E}$ field contributions are expected to have larger errors, and the potential might be too high for large R/a.

3.2.3 Potentials

Compared to the calculation of the $\beta = 2.5$ case, the operators $\mathbf{R}\cdot(\mathbf{R}\times\mathbf{E})$ and $\mathbf{R}\times(\mathbf{R}\times\mathbf{E})$ are not considered, since their effective masses could not be analyzed for sufficient large temporal extension. Fig. 3.8 shows the computed static hybrid potentials for $\beta = 2.7$. Remarkable is the discrepancy of the two Σ_g^+ states (green and yellow curve). As mentioned before, this could be a consequence from fitting the effective potential before it has reached the plateau.

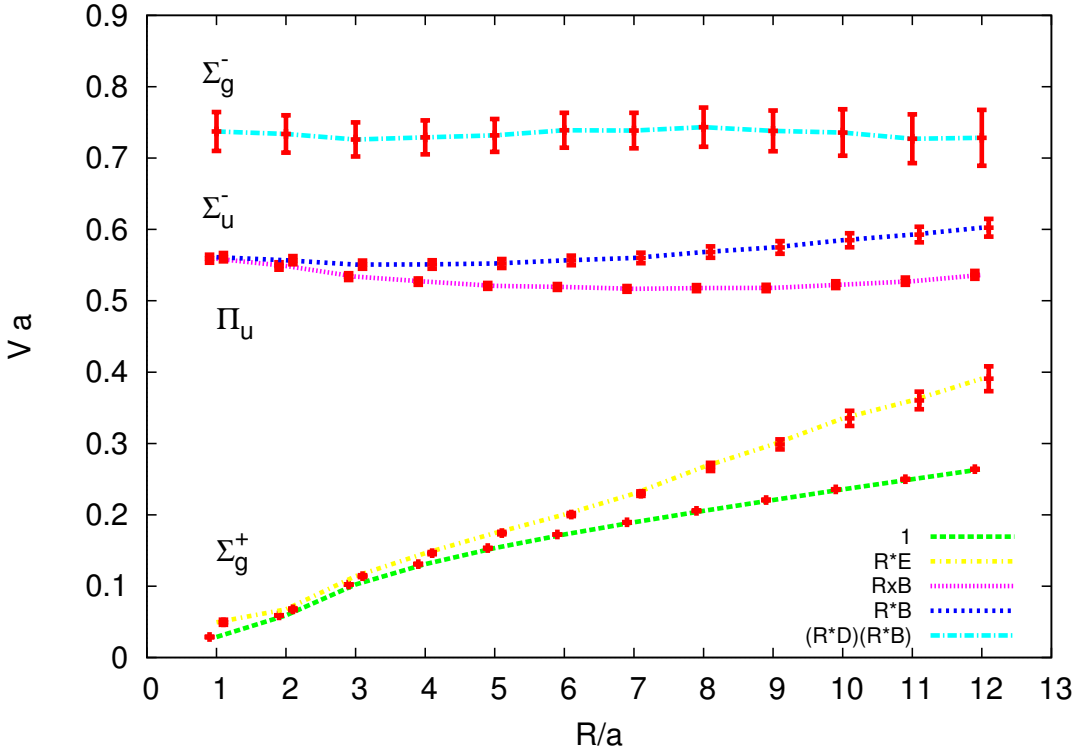

Figure 3.8: Hybrid static potentials in SU(2) Yang-Mills theory in units of the lattice spacing ($a \approx 0.038$ fm). *To be able to distinguish between the different curves, the errorbars have slightly been shifted horizontally.*

3.3 Comparison of the $\beta = 2.5$ and $\beta = 2.7$ computations

In order to compare both calculations, they have to be rescaled to physical units. But still, the potentials from the $\beta = 2.7$ computation should be shifted upwards compared to the ones with $\beta = 2.5$. For the case of the $\beta = 2.7$ calculation (smaller lattice spacing), the static quarks are more localized, which leads to higher self energy contributions compared to the first calculation with the larger lattice spacing. Therefore, all potentials have to be shifted equally in order to compare both results.
On the one hand, the comparison shall verify the correctness of the computations, and on the other, the short distance behavior of the hybrid potentials shall be investigated. Of particular interest is the Π_u state, which indicates to be repulsive for small spatial separations. Since for small separations cut-off effects can be present, it is not clear, if the observed repulsive behavior is a physical feature or merely caused by the cut-off.

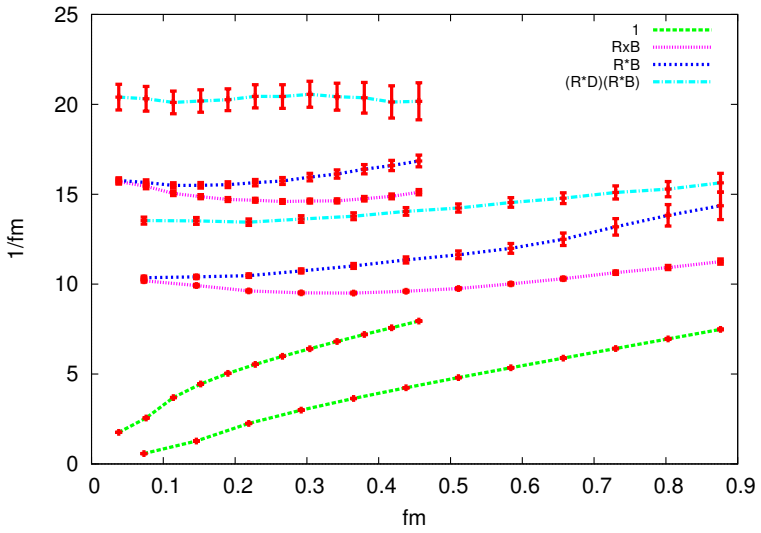

Figure 3.9: The static hybrid potentials from the gluonic operators: 1, $\mathbf{R} \times \mathbf{B}$, $\mathbf{R} \cdot \mathbf{B}$ and $(\mathbf{R} \cdot \mathbf{D})(\mathbf{R} \cdot \mathbf{B})$ for $\beta = 2.5$ and $\beta = 2.7$, in physical units. The hybrid potentials which have separations of ≈ 0.03 fm$\ldots$0.45 fm correspond to the $\beta = 2.7$ computation, in which the lattice spacing was identified with 0.038 fm.

Fig. 3.9 shows the static hybrid potentials of the states Σ_g^+, Π_u, Σ_u^- and Σ_g^- for the two different β-values in physical units. As mentioned before the curves are still shifted by the self energy contributions. This shift is expected to be equal for all potentials. Having a closer look at fig. 3.9, one notices that the shift of the hybrid potentials is

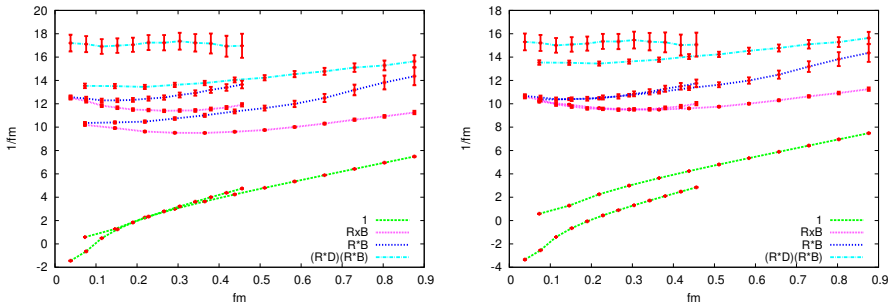

Figure 3.10: The potentials of the $\beta = 2.7$ have been shifted with -2.2 1/fm **(left)**, in this case the ordinary static potentials match, and -4.1 1/fm **(right)**, for which the hybrid potentials are equal within errors.

roughly two times bigger than the one of the ordinary static potential. In fig. 3.10 two different shifts can be seen. In the first case (left plot), the shift is performed in a way that the ordinary potentials of both calculations match, and on the right side, the hybrid potentials are equal.
At the moment, it is not completely clear why not all potentials are equally shifted. In the following, possible explanations will be discussed.

Not sufficiently large enough temporal extensions for the $\beta = 2.7$ calculation. Since the effective masses could not be analyzed for the same temporal distance as in the first computation, they could still be dominated by excited states. This could cause that the potentials are too high.
To investigate this, the effective potentials of the $\beta = 2.5$ calculation were fitted in the same physical range, i.e. $T/a = 3 \ldots 4$. Therefore both computations should have about the same contributions from excited states. But it became apparent, that this effect is rather small and cannot completely explain the discrepancy of the shifts.

Uncertainty of the lattice spacing a for $\beta = 2.7$. The determination of the lattice spacing gets more difficult for higher values of β, as much larger lattices have to be considered to be able to reach the linear region of the static potential, which is then identified with the string tension. If we assume that the lattice spacing of $\beta = 2.7$, which was set to $a = 0.038$ fm, is subject to some uncertainty, one could vary the lattice spacing in order to achieve an equal shift for all potentials. This also suggests a possible method to determine the lattice spacing. Fig. 3.11 shows the potentials for the case that the lattice spacing, which corresponds to

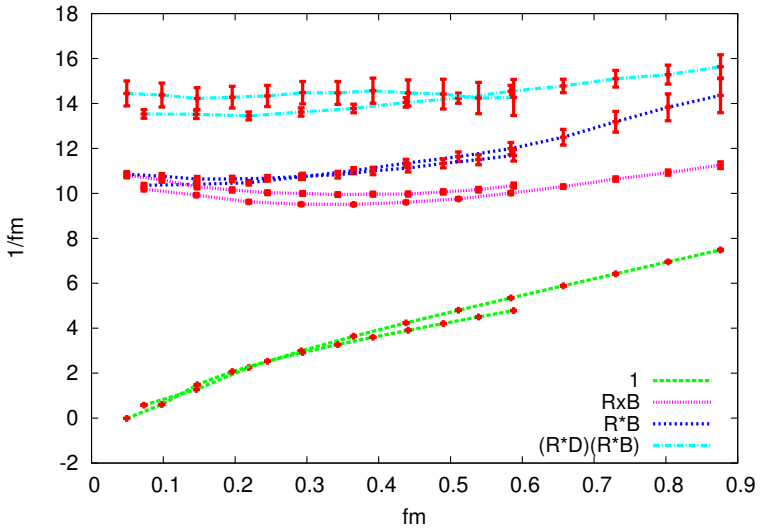

Figure 3.11: The lattice spacing of the $\beta = 2.7$ computation has been changed to $a = 0.049$ fm, while $a = 0.073$ for the $\beta = 2.5$ calculation.

$\beta = 2.7$, has been changed to $a = 0.049$ fm, while the other lattice spacing is still $a = 0.073$ fm. The change of the lattice spacing is almost 30% compared to the former value, which seems to be rather high, and furthermore, for large separations the ordinary potential from the $\beta = 2.7$ computation is slightly below the ordinary potential from the first calculation. But actually it is expected that it should be slightly above, since excited states should rather be involved in the $\beta = 2.7$ calculation.

In conclusion, none of the suggested explanations completely justifies the discrepancy of the shifts. If one can still believe the results, the computations support the thesis that the repulsive behavior of the Π_u hybrid is truly a physical feature. Both calculations of Π_u indicated a repulsive shape. If both curves are shifted onto each other, like in fig. 3.10 (right), they even match for small separations, which indicates that no cut-off effects appear. Of course, this statement has to be treated with caution, until the reason for the different shifts of the ordinary potential and the hybrids is understood.

4 Conclusion

4.1 Summary

Four static hybrid potentials, Σ_g^+, Π_u, Σ_u^- and Σ_g^-, were computed for the two lattice spacings $a \approx 0.073$ fm and $a \approx 0.038$ fm. For this purpose, ten different gluonic creation operators were calculated, from which seven could be evaluated. The signal of the remaining operators did not allow a reasonable analysis.
Moreover, the correlation functions were cross-checked for parity, time reversal and separation axis symmetries, whereby no disagreements could be detected.
Except for the different shift of the ordinary potential compared to the hybrid potentials, which was found by comparing the two computations with different lattice spacings, the results are in agreement with our expectations. Furthermore, the results are consistent with earlier studies, e.g. [11].
For the Π_u hybrid potential some indication for a repulsive behavior at short separations could be found.

4.2 Outlook

It will be necessary to understand the origin of the different shifts, which have been discussed before. On the one hand, this would be an additional confirmation for the correctness of the computations, and on the other, it would allow a more precise analysis concerning the short distance behavior of Π_u.
Since our results have much larger errors compared to other studies, e.g. [11], it could be possible that the considered operators, which contain local insertions of chromomagnetic or chromoelectric field operators, have a poor ground state overlap. In [6, 8] non-local operators are suggested, which may result in having smaller statistical errors. However, a further analysis with the operators used in this work involving more computation time seems not reasonable. Due to the unfavorable signal-to-noise ratio, a significant improvement of the results will not be feasible. Therefore, an implementation of more

extended operators should be explored. Moreover, smearing techniques can be applied in order to optimize the spatial shape and extension of the creation operators with respect to the considered ground state.
The ultimate goal is, of course, to arrive at precise results for SU(3) Yang-Mills theory and QCD. This would allow to estimate masses of hybrid mesons by solving a non-relativistic Schrödinger equation with the computed hybrid static potentials, as e.g. proposed in [3, 4, 6, 8, 12, 13, 14].

References

[1] W. M. Yao *et al.* [Particle Data Group Collaboration], J. Phys. G **33**, 1 (2006).

[2] K. J. Juge, J. Kuti and C. J. Morningstar, Nucl. Phys. Proc. Suppl. **63**, 326 (1998) [hep-lat/9709131].

[3] M. J. Peardon, Nucl. Phys. Proc. Suppl. **63**, 22 (1998) [hep-lat/9710029].

[4] K. J. Juge, J. Kuti and C. J. Morningstar, AIP Conf. Proc. **432**, 136 (1998) [hep-ph/9711451].

[5] C. Morningstar, K. J. Juge and J. Kuti, hep-lat/9809015.

[6] C. Michael, Nucl. Phys. A **655**, 12 (1999) [hep-ph/9810415].

[7] D. Toussaint, Nucl. Phys. Proc. Suppl. **83**, 151 (2000) [hep-lat/9909088].

[8] C. Michael, PoS **HeavyFlavours8**, 001 (1999) [hep-ph/9911219].

[9] G. S. Bali *et al.* [SESAM and TχL Collaborations], Phys. Rev. D **62**, 054503 (2000) [hep-lat/0003012].

[10] C. Morningstar, AIP Conf. Proc. **619**, 231 (2002) [nucl-th/0110074].

[11] K. J. Juge, J. Kuti and C. Morningstar, Phys. Rev. Lett. **90**, 161601 (2003) [hep-lat/0207004].

[12] C. Michael, hep-lat/0302001.

[13] K. J. Juge, J. Kuti and C. Morningstar, AIP Conf. Proc. **688**, 193 (2004) [nucl-th/0307116].

[14] C. Michael, hep-ph/0308293.

[15] G. S. Bali and A. Pineda, Phys. Rev. D **69**, 094001 (2004) [hep-ph/0310130].

[16] N. Brambilla, A. Pineda, J. Soto and A. Vairo, Rev. Mod. Phys. **77**, 1423 (2005) [hep-ph/0410047].

[17] HJ Rothe: An introduction to lattice gauge theories

[18] Gattringer, Lang: Introduction to lattice gauge theory

[19] O. Philipsen and M. Wagner, Phys. Rev. D **89**, 014509 (2014) [arXiv:1305.5957 [hep-lat]].

[20] M. Wagner, S. Diehl, T. Kuske and J. Weber, arXiv:1310.1760 [hep-lat].

[21] G. S. Bali *et al.* [SESAM Collaboration], Phys. Rev. D **71**, 114513 (2005) [hep-lat/0505012].

[22] M. Wagner [ETMC Collaboration], PoS LATTICE **2010**, 162 (2010) [arXiv:1008.1538 [hep-lat]].

[23] O. Andreev, Phys. Rev. D **86**, 065013 (2012) [arXiv:1207.1892 [hep-ph]].

[24] Peskin Schröder: Introduction to Quantumfield Theory

Danksagung

Insbesondere möchte ich Prof. Marc Wagner für eine ausgezeichnete Betreuung mit zahlreichen wertvollen Gesprächen danken.
Außerdem möchte ich mich bei Joshua Berlin für die Unterstützung mit den Großrechnern Loewe und Fuchs bedanken.
Zuletzt gilt besonderer Dank meinen Kommilitonen Annabelle Uenver-Thiele, Björn Wagenbach und Constantin Butzke, die mich nicht nur während der Masterarbeit, sondern auch in den letzten Jahren immer unterstützt haben.